Research Square

Preprints are preliminary reports that have not undergone peer review.
They should not be considered conclusive, used to inform clinical practice,
or referenced by the media as validated information.

A Novel Methodology for the Evaluation of Adapt-to-Position Segment Shape Optimisation in MR-Guided Radiotherapy

Marchant Van der Walt

marchant.vanderwalt@health.qld.gov.au

Townsville Hospital

Rick Franich

RMIT University

John Baines

Townsville Hospital

Research Article

Keywords: MR-linac, Adaptive radiotherapy, Adapt to position, Segment shape optimisation, Quality assurance, Phantom dosimetry

Posted Date: November 23rd, 2026

DOI: https://doi.org/10.21203/rs.3.rs-11688388/v1

License: This work is licensed under a Creative Commons Attribution 4.0 International License.
Read Full License

Additional Declarations: No competing interests reported.

A Novel Methodology for the Evaluation of Adapt-to-Position Segment Shape Optimisation in MR-Guided Radiotherapy

Abstract

Daily MR guided adaptive radiotherapy represents the current pinnacle of image guidance sophistication in external beam radiotherapy. In this work, we present a novel methodology for the quantitative assessment of the Elekta Unity MR Linac (Elekta AB, Stockholm, Sweden) Adapt to Position (ATP) Segment Shape Optimisation (SSO) planning algorithm as used in a clinical environment. MR-safe positioning devices manufactured via 3D printing were used to precisely offset a phantom in known increments along each axis of the IEC 61217 coordinate system. Ion chamber and radiochromic film (RCF) measurements were used to compare adaptive algorithm dosimetry and field repositioning at these offset positions compared to a phantom reference position. The registration read back 12 known spacer offsets within 0.6 mm. Without adaptation, the chamber detected offsets of 2 mm along x (3 mm on an older plan) and 3 mm along y and z. For 42 SSO adaptations (5–30 mm) the chamber read +0.2% (SD 0.6%) against the calculated dose to water; 3 points lay outside ±1.1% and one at 2.03 standard uncertainties of its own budget (k = 2). The plan-side gamma pass rate fell as the apertures departed from a pure translation (rho = −0.81, 33 plans); the chamber did not resolve this. All film comparisons passed a global 2%/2 mm gamma criterion. It may be concluded that the ATP SSO algorithm delivered the adapted calculated dose within the per-point uncertainty at 41 of 42 points, and that the chamber alone cannot resolve errors below 2 to 3 mm.

Keywords: MR-linac · Adaptive radiotherapy · Adapt to position · Segment shape optimisation · Quality assurance · Phantom dosimetry

Introduction

Adaptive radiotherapy has emerged as a powerful approach to improving treatment precision and reducing normal tissue toxicity through daily plan modification in response to changes in patient anatomy and positioning [1-4]. Conventional image guided radiotherapy (IGRT) corrects for setup error through mechanical couch adjustments, typically using six degrees of freedom (6DoF), combined with image registration between on-board cone-beam computed tomography (CBCT) and the planning CT [5-9]. While this approach effectively reduces patient positioning uncertainty [8,9], it does not address anatomical variations in tumour position and/or shape that may occur during the course of treatment [10-12]. In addition, repeated CBCT-based imaging contributes an incremental imaging dose over the treatment course [5], an issue that is inherently mitigated in MR-guided radiotherapy (MRgRT) where daily imaging is performed without ionising radiation.

MRgRT addresses these limitations by providing superior soft-tissue contrast without the use of ionising radiation, enabling precise anatomical visualisation of the target and organs at risk (OARs) at each fraction throughout the course of treatment [11-14]. This improved soft-tissue visualisation allows for daily plan adaptation using either Adapt to Position (ATP) and/or Adapt to Shape (ATS) workflows, thereby enabling treatment to be tailored to the patient's anatomy on the day of treatment.

The Elekta Unity MR-linac (MRL) integrates a 7 MV flattening filter free (FFF) linear accelerator with a 1.5 T Philips MR system (Philips Healthcare, Amsterdam, The Netherlands), providing real-time MR imaging with simultaneous radiation delivery [15-19]. The integration of MRI requires a relatively narrow MRI bore around the patient couch and introduces a constraint to the conventional image-guided patient setup workflow. In particular, the movement of the patient couch is limited to longitudinal shifts: lateral and vertical couch shifts are not possible. In practice, registration of patient position to the treatment plan based on in situ imaging is achieved by virtual couch shifts [20]. These are implemented by adapting the multi-leaf collimator (MLC)-defined field positions in lieu of couch movements. In the Elekta system, this plan adaptation is known as adapt to position (ATP).

As the superior soft tissue contrast of MR imaging allows for better tumour/target visualisation, positional registration can more frequently be based on the target rather than anatomical surrogates such as bony anatomy and body contours. As such, ATP can simultaneously be used to compensate for changes in the internal position of the target relative to the reference anatomy. The ATP workflow retains the contours of the original plan. If the daily imaging warrants re-contouring, the adapt to shape (ATS) workflow is used, which fundamentally starts with an ATP step to account for positional offset. Specifically, ATP achieves this repositioning through Segment Shape Optimisation (SSO), whereby the shape of each MLC-defined treatment field is reshaped to reflect the calculated positional offset; it is this SSO process that is the specific focus of the present work.

The accuracy of the resulting ATP SSO adaptation is therefore governed by several interlinked sources of uncertainty. First, the calculated positional offset depends on the accuracy of image registration between the daily MR and the reference CT, which is subject to residual CT–MR fusion error and to geometric distortion inherent to MR imaging arising from gradient non-linearities and susceptibility effects [20-23]. Second, this offset must be correctly translated into a corresponding reshaping of the MLC-defined segments, within the physical constraints imposed by leaf width and leaf-edge positioning. Third, the segment weighting may require adjustment to preserve the intended beam profile and dose distribution following reshaping, particularly where the internal displacement of the target differs from the applied virtual couch shift.
Consequently, rigorous experimental verification of the ATP SSO workflow requires assessment of three distinct components: (R1) the accuracy of the image registration underpinning the calculated positional offset; (R2) the fidelity with which this offset is translated into segment repositioning via SSO; and (R3) confirmation that the resulting adapted plan delivers the intended dose distribution. It is this need for a comprehensive, quantitative assessment, spanning both geometric and dosimetric domains, that motivates the methodology described in this work.

The aim of this study was to develop and validate a robust, reproducible methodology for evaluating the geometric and dosimetric performance of the Unity adaptive radiotherapy workflow, with a particular focus on ATP. This framework is designed to comprehensively assess the accuracy and consistency of plan adaptation, ensuring that both geometric precision and dosimetric fidelity are maintained in a clinically relevant context. The phantom and the spacer adjusters are shown in Figure 1, and the inserts in Figures 3–5.

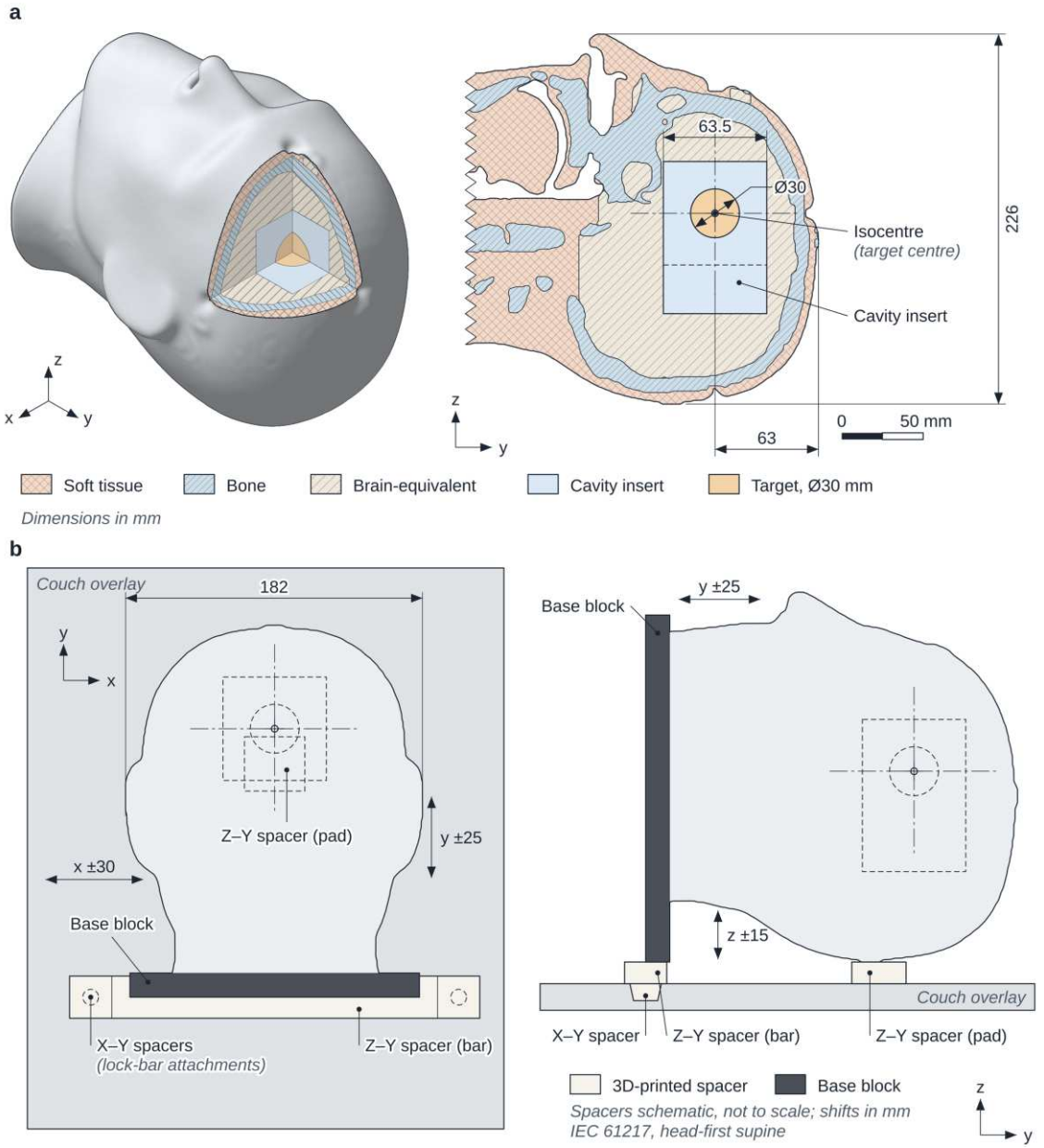


Fig. 1 The STEEV2 head phantom and the spacer adjusters used to offset it on the couch overlay. (a) Cut-away rendering of the phantom (one octant removed) showing the soft tissue, bone and brain-equivalent layers, the cavity insert and the 3 cm target sphere, and a mid-sagittal section through the isocentre, which is at the centre of the target. The cavity insert, 63.5 mm wide, holds the Ø30 mm target; the inserts are shown in Figs. 3–5. (b) Plan view (x and y) and side view (z and y) of the phantom on the couch overlay. The head is mounted on its base block, which stands on a Z–Y spacer bar across the couch; the X–Y spacers (lock-bar attachments) at the ends of the bar are keyed into the couch index holes, and a second Z–Y spacer lies under the occiput. The arrows give the ranges of the offsets used (x ±30 mm, y ±25 mm, z ±15 mm). The phantom is drawn to scale from the reference CT; the spacers and the base block are schematic. The IEC 61217 axes for head-first supine are x to the patient's left, y towards the head and z upward. Dimensions in mm.

Materials and Methods

2.1 MR-Linac

All measurements were performed on a clinical Elekta Unity MR-linac (Elekta AB, Stockholm, Sweden). Intensity-modulated radiotherapy (IMRT) treatment plans were generated using the Monaco treatment planning system (TPS) v5.51.11 (Elekta AB, Stockholm, Sweden), with Monte Carlo dose uncertainty set at 3% per control

point with a 2 mm dose grid. The Unity platform employs a fixed longitudinal couch position determined at simulation, with soft tissue alignment performed through rigid image registration (RIR) of daily MR imaging with a reference CT data set. The adaptation workflow was conducted under standard clinical conditions as defined by the vendor. A schematic cross section of the Elekta MRL is shown below (Figure 2) providing additional information on the system. For further technical details of the Unity system, the reader is referred to existing dedicated system descriptions [13,21,22].

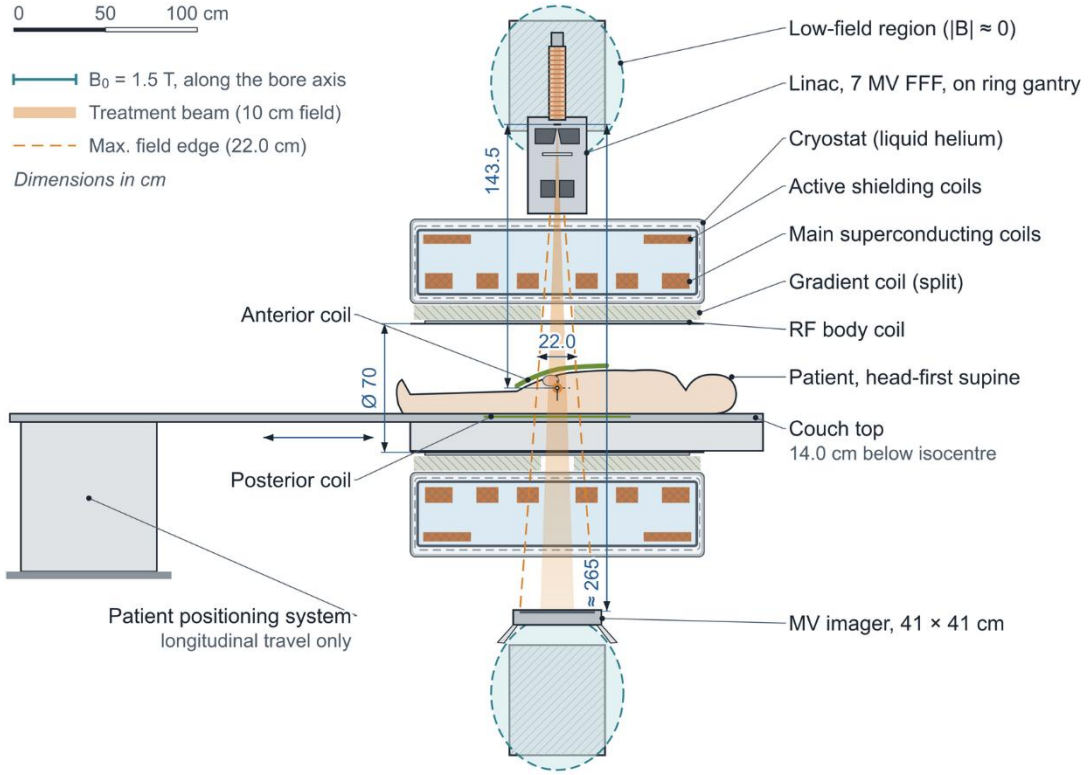


Fig. 2 Schematic longitudinal section of the Elekta Unity MR-Linac through the bore axis, in the gantry 0°/180° plane, with the patient head-first supine. The 7 MV FFF linac is mounted on a ring gantry in the low-field region outside the 1.5 T magnet. The beam passes between the halves of the split gradient coil and between the main superconducting coils, reaching the isocentre at 143.5 cm from the source and the megavoltage imager at approximately 265 cm. The bore diameter, source distances, tabletop height and maximum in-plane field are drawn to scale; the magnet internals are schematic. Dimensions in cm.

2.2 Phantom and Setup

A STEEV2 anthropomorphic head phantom (CIRS Inc., Norfolk, VA, USA), originally developed for end-to-end stereotactic verification, was repurposed in this study to evaluate the geometric and dosimetric performance of the ATP workflow. Known physical shifts were introduced to the phantom and compared against the corresponding ATP-derived corrections based on MR imaging, with dosimetric performance assessed relative to the reference position under controlled conditions. The phantom contains a cavity into which various modules can be inserted, including: (a) isomorphic structures representative of clinical target volumes, (b) a custom insert for a PTW PinPoint ionisation chamber, and (c) a split cube to accommodate film (see Figures 3–5). The target was a 3 cm sphere contoured on the reference CT, and the MR-visible liquid-fillable insert was a 3 cm sphere. The chamber was used in its plug insert, which is the insert represented in the TPS. Positioning of the phantom was

achieved using a lock bar, and a series of 3D printed slabs of known dimensions was used to introduce various shifts of the phantom relative to a reference position (0,0,0) (Figure 6).

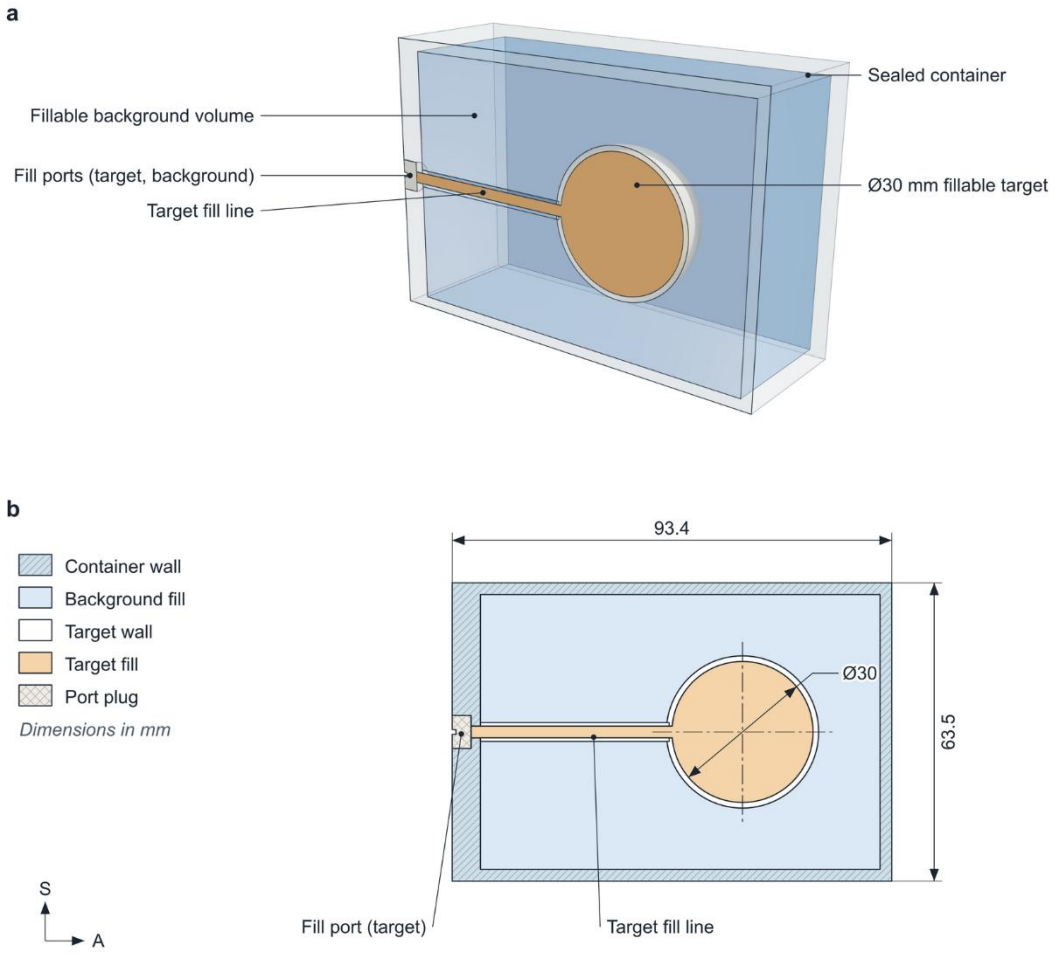


Fig. 3 Imaging insert of the STEEV2 phantom with the liquid-fillable spherical target. (a) Cut-away rendering. (b) Mid-sagittal section. The Ø30 mm target and the background volume are filled separately through the fill ports. Dimensions in mm.

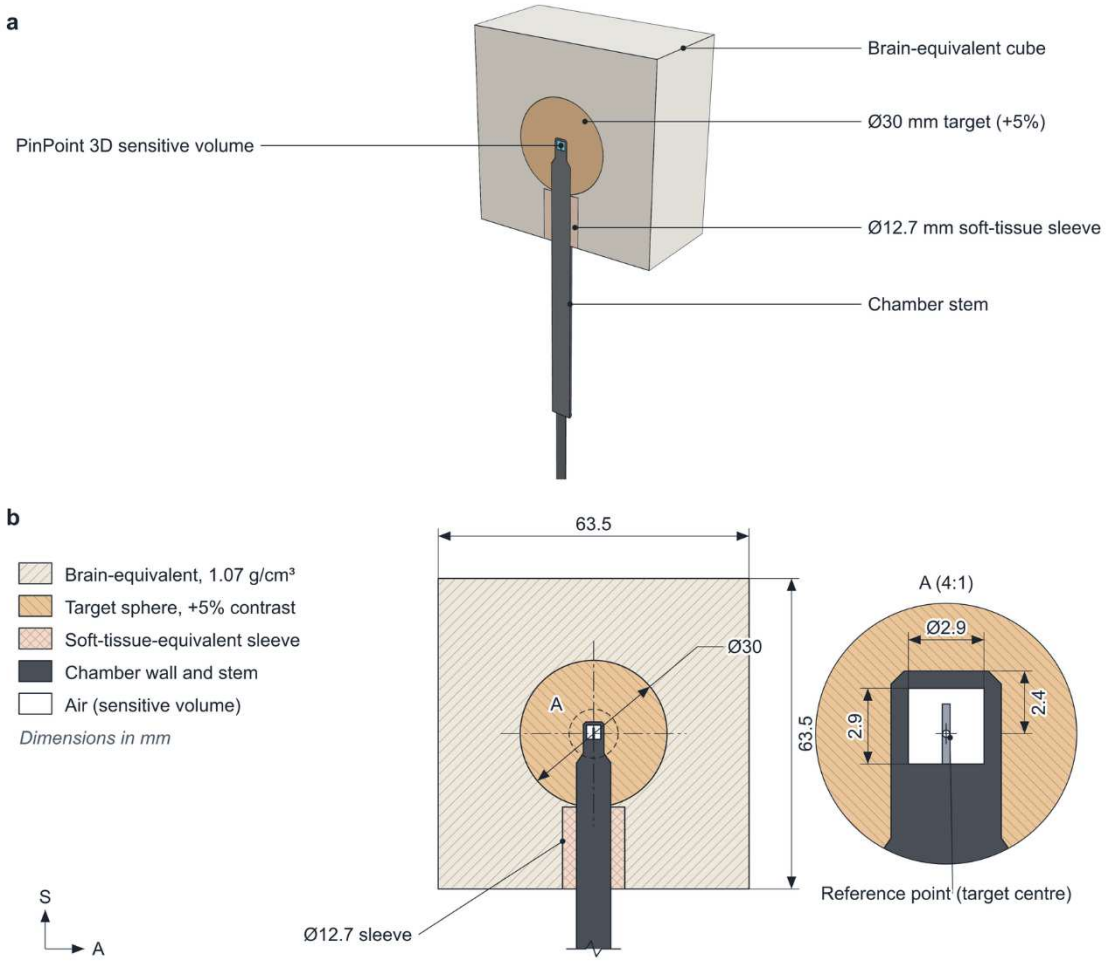


Fig. 4 Chamber insert of the STEEV2 phantom, machined for the PTW PinPoint 3D chamber. (a) Cut-away rendering at the mid-sagittal plane. (b) Mid-sagittal section. Detail A (4:1) shows the Ø2.9 × 2.9 mm sensitive volume, with the chamber reference point 2.4 mm from the tip and positioned at the centre of the Ø30 mm, +5% contrast target. The soft-tissue-equivalent sleeve fills the Ø12.7 mm inferior–superior channel. Dimensions in mm.

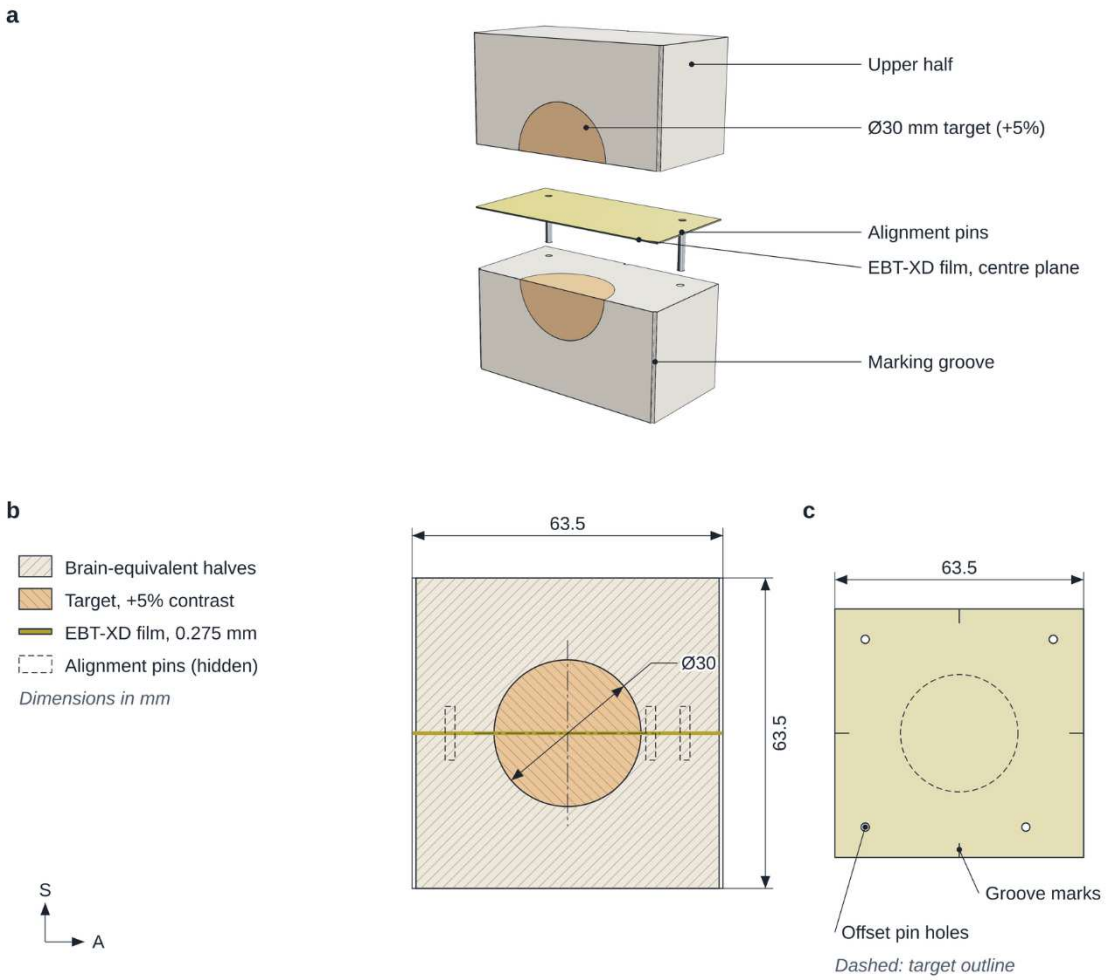


Fig. 5 Film insert (split cube) of the STEEV2 phantom. (a) Exploded cut-away rendering showing EBT-XD film in the centre plane of the Ø30 mm, +5% contrast target, between two brain-equivalent halves located by offset alignment pins. (b) Mid-sagittal section with the film in the axial orientation. (c) Film-plane view from superior, showing the pin holes, groove marks and target outline. Dimensions in mm.

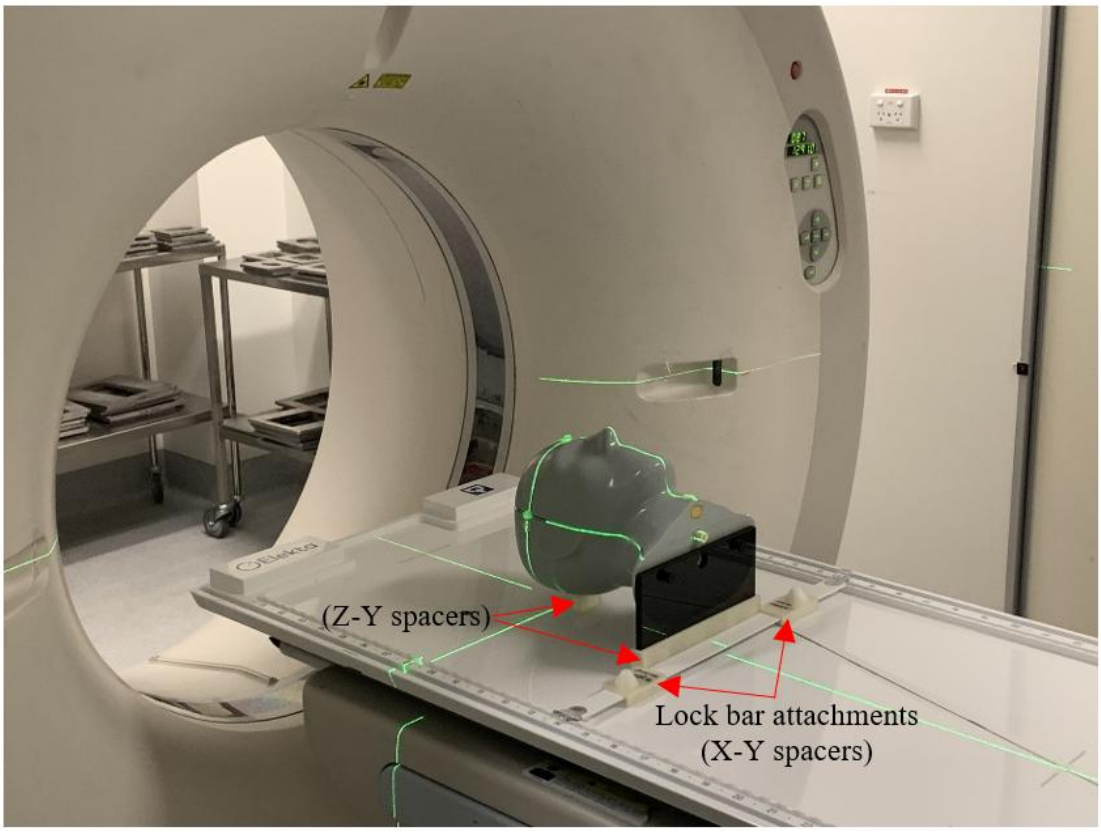


Fig. 6 STEEV2 phantom CT setup using MRL couch overlay and 3D printed attachments for reproducible setup at the Townsville Cancer Centre (TCC)

2.3 Imaging and Planning Workflow

A reference CT image dataset of the STEEV2 phantom was acquired on a Toshiba Aquilion scanner (Canon Medical Systems, Otawara, Japan) using a clinical 1 mm slice thickness brain protocol and transferred to the Monaco treatment planning system (TPS) for treatment plan generation. A 9-field step-and-shoot IMRT plan was generated on this initial CT dataset and served as the reference for future adaptations. The beams were at gantry angles 0, 40, 80, ... 320 degrees (the setup on the reference CT is shown in Fig. S1 of Online Resource 1). The Monaco objectives (Table S1 in Online Resource 1) were a target-penalty objective on each of three sphere structures (Smallsphere2, SmallSphere and Sphere2; isoconstraints 6, 4 and 2 as displayed), each with a quadratic-overdose objective at 6.1, 4.1 and 2.1 Gy, and three objectives on the external contour. Sequencing used segment shape optimisation with high-precision leaf positions, a minimum segment area of 2 cm² and width of 0.5 cm, low fluence smoothing, at least 2 monitor units (MU) per segment and at most 250 segments. The top-hat field was not used. The TPS dose at the chamber point was about 6.3 Gy. A corresponding reference MR dataset was acquired on the Elekta Unity system using a Philips T1 3D Brain turbo field echo (TFE; ultrafast gradient echo) sequence (Table 1). These reference CT and MR datasets, acquired with the phantom in a defined baseline position, were used to establish the reference planning geometry.

RIR of CT–MR was performed in the online Monaco TPS to align the reference phantom datasets (Figure 7). The registration was a manual user match of the CT sphere contour to the liquid-filled sphere on the MR image, with translations only (no rotations), because ATP corrects translation. The residual of the match was not recorded; the reproducibility of the registration at the baseline position (±0.5 mm, k = 2, see Results) is taken as its uncertainty.

To evaluate the ATP workflow, additional MR images were then acquired either with the phantom in the baseline position or after introducing known geometric offsets. For each fraction, ATP plans were generated by fusing the reference CT with the on-board MR image, applying RIR-based shifts, and recalculating the plan according to the ATP workflow.

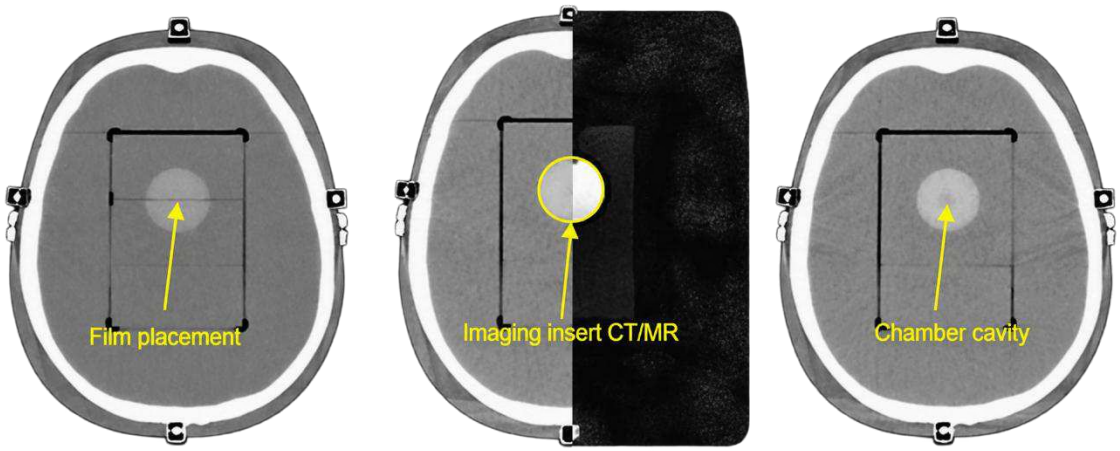


Fig. 7 CT of film dosimetry insert (left), CT-MR fusion of liquid fillable insert (mid), ionisation chamber insert (right)

Table 1 MR scanning parameters. BW: bandwidth; NSA: number of signal averages; SENSE: sensitivity encoding; TFE: turbo field echo.

Philips T1 3D Brain TFE (ultrafast gradient echo)	
Repetition time	8.0 ms
Echo time	3.6 ms
Slice thickness	2.2 mm
Matrix	256×182×182
BW (Hz/pixel)	246.6
SENSE factor (p reduc)	1.3
Receiver coils	Anterior & Posterior
NSA	1
Voxel size	0.8 mm

2.4 Geometric Offset

Phantom displacements were introduced using 3D-printed spacers manufactured from a thermoplastic previously found to be safe for use in external beam dosimetry (polylactic acid, PLA) [24]. Offsets of 1 to 5 mm in 1 mm steps were applied with the plan not adapted, to test the sensitivity of the chamber. For ATP, offsets were multiples of 5 mm along the lateral (x), longitudinal (y), and vertical (z) axes, up to 30 mm along x, 25 mm along y and 15 mm along z for the chamber measurements. Additional measurements were performed with combination offsets along multiple axes to evaluate the performance of the ATP algorithm under more complex geometric perturbations. All offsets were verified using physical measurements and independent image review. The maximum offset magnitude was chosen based on a statistical analysis of CT–MR registration offsets observed in the first 10 prostate patients (about 20 fractions each) treated on the MRL at our facility.

2.5 *Dosimetric Measurements*

2.5.1 *Ion Chamber Dosimetry*

Absolute dose verification for each phantom configuration (baseline and offset positions) was performed using an MR-conditional PTW 3D PinPoint ionisation chamber (model 31022) with an active volume of 0.016 cm^3, in its plug insert, cross-calibrated against a reference MR-conditional PTW Farmer chamber (model 30013) following published correction protocols for magnetic field dosimetry [25,26]. The chamber was positioned at the central axis (CAX) under baseline conditions, and measurements were then repeated for each offset scenario. Measured doses (the corrected readings of the measurement workbook) were compared against Monaco TPS predictions at corresponding positions and against reference chamber measurements. The TPS dose compared with the chamber is dose to water: the dose to medium of the plan multiplied by 1.006, the medium-to-water factor of the phantom material. The TPS value is the mean dose over the chamber cavity (the DICOM dose averaged over a cylinder of the cavity size reproduces it to −0.03%, SD 0.21%, n = 48 plans). Of the adaptations with a chamber reading, 42 used SSO; two used other methods (segment aperture morphing, SAM: morph only; segment weight optimisation, SWO: morph and weight optimisation) and are reported separately.

2.5.2 *Radiochromic Film Dosimetry*

Gafchromic EBT-XD film (Ashland Advanced Materials, Bridgewater, NJ, USA) was used to provide high-spatial resolution dose measurements. Films within the STEEV2 split cube insert were positioned in the coronal, sagittal, and transverse planes and the treatment beam was delivered. For each phantom position the exposed film was scanned on an Epson Expression 12000XL flatbed scanner at 75 dpi following a 24-hour development period. Film analysis was performed in FilmQA Pro (Ashland) using triple channel analysis, with dose calibration curves derived from reference exposures using rational functions per Lewis and Chan [27]. Three fiducial marks were made by hand on each film, each with an uncertainty of about 0.25 mm, and the film was registered to the TPS dose export of its plane through them, not by matching the dose distributions. Film-to-TPS and film-to-film gamma analyses were conducted with a global 2%/2 mm criterion, a 10% low-dose threshold and dose normalised to the maximum dose. The film-to-film comparisons used the maximum offset on all three adjusters, 30 mm in x, 30 mm in y and 15 mm in z.

2.5.3 *Plan-side Checks*

The plan-side checks of the aperture positions and the whole-volume comparison are described and reported in Online Resource 1.

2.6 *Uncertainty Characterisation*

Geometric uncertainty sources included:

- CT–MR fusion uncertainty (± 0.5 mm)
- MR geometric distortion (± 0.47 mm, annual MR-linac quality assurance (QA))
- Couch position reproducibility (± 0.2 mm, monthly couch QA)
- Spacer fabrication tolerances (± 0.4 mm)
- Film fiducial marking (± 0.25 mm per mark, 3 marks)

Dosimetric uncertainty sources included:

- Ionisation chamber measurement uncertainty (± 1.1%)
- TPS Monte Carlo statistical uncertainty of each point (0.5 to 1.8% for the 42 SSO offsets)
- Film dose uncertainty (about 3%)

Geometric uncertainties were combined in quadrature; all values except the two film estimates have a coverage factor k = 2. The chamber uncertainty of ±1.1% combines the calibration certificate of the Australian Radiation Protection and Nuclear Safety Agency (ARPANSA) of the secondary-standard Farmer chamber and the cross-calibration to the PinPoint chamber: 0.911% (calibration and user beam, in quadrature) plus 0.2% (cross-calibration) added linearly, a deliberate conservative choice (in quadrature: 0.93%). The uncertainty of a chamber minus TPS difference at one point is the chamber term and the TPS statistical term of that point (the workbook standard deviation over the dose, taken as one standard deviation and doubled) in quadrature (1.2 to 2.1%, median 1.4%, for the 42 SSO offsets), with no volume term because the TPS value is the cavity mean.

2.7 *Data Analysis*

Ionisation chamber data was evaluated as percent difference from TPS predictions under baseline and offset conditions. Film data was analysed through 2D gamma index comparison to quantify geometric and dosimetric agreement under both baseline and ATP-corrected offset scenarios. Gamma pass rates and dose difference distributions were used to evaluate the sensitivity and robustness of the ATP workflow in compensating for daily geometric shifts. All statistical results were reported with k = 2 coverage where applicable. The chamber difference is (measured − TPS)/TPS with the TPS dose to water. Each point was judged against its own uncertainty U by zeta = difference/(U/2). The baseline set is the 16 readings at the reference position (18 baseline entries; one deliberately offset in y and one without a chamber reading were not used). Offsets were compared with the baselines by Welch's test, and registration shifts are taken relative to the baseline of the same session. The detection limit is the smallest tested offset at which the reading falls by more than the ±1.1% band.

Results

Experiment uncertainty

The reproducibility of the CT–MR fusion process using the STEEV2 phantom was measured as ±0.5 mm (k = 2, 95% coverage interval; twice the SD of the registration shift over the 16 baseline setups, largest axis). MR geometric distortion contributed an additional ±0.47 mm, while the accuracy of 3D-printed spacers and couch position reproducibility were ±0.4 mm and ±0.2 mm, respectively. When combined in quadrature, the total geometric uncertainty was determined to be ±0.82 mm (k = 2). In addition to geometric factors, dosimetric uncertainties were also quantified. The uncertainty associated with the primary standards dosimetry laboratory (PSDL) calibration was 0.648%, while uncertainties related to the user beam and cross-calibration contributed 0.640% and 0.2%, respectively. Combining these components, with the cross-calibration added linearly, resulted in a total estimated dose uncertainty of 1.1% (k = 2). A complete summary of both geometric and dosimetric contributions is provided in Table 2.

The registration detected every applied offset. Twelve readings of known spacers (from 11 registrations, each paired with the baseline reading that precedes it) differed from the nominal offset by −0.6 to +0.3 mm (mean −0.1 mm, SD 0.2 mm; largest 0.6 mm); this is the evidence for R1. For the 44 ATP adaptations with a chamber reading (57 non-zero axis components), the shift reported by the registration differed from the nominal offset by −0.4 to +0.5 mm (mean +0.1 mm, SD 0.3 mm). All ATP spacer offsets were multiples of 5 mm, so the nominal offset of

each adaptation is the registration reading rounded to the nearest 5 mm; this is a consistency check and adds no independent evidence. The registration reads about −1.9 mm in y and −1.2 mm in z at the reference position (mean of the 16 baselines), so shifts are taken relative to the baseline of the session.

Table 2 Summary of geometric and dosimetric uncertainty sources contributing to total system uncertainty. Values are reported with coverage factor k = 2 (the film fiducial estimate is the authors' estimate, k not stated).

Sources of experimental uncertainty (k = 2, 95% coverage interval)	
CT-MR fusion reproducibility – STEEV2	± 0.5 mm
MR geometric distortion (site QA)	± 0.47 mm
Accuracy of 3D printed spacers	± 0.4 mm
Couch position reproducibility (site QA)	± 0.2 mm
Total geometric uncertainty	**± 0.82 mm**
Film fiducial marking, per mark (3 marks; not in the total)	± 0.25 mm
Uncertainty PSDL	0.648%
Uncertainty User beam	0.640%
Uncertainty Cross calibration (added linearly)	0.2%
Total estimated dose uncertainty	**1.1%**

Chamber measurements

The response of the 3D PinPoint ionisation chamber to systematic phantom offsets, with the plan not adapted, is shown in Figure 8 and Table 3. Chamber readings were normalised to the CAX measurement of the same plan (reference position (0,0,0)) and plotted as a function of phantom displacement along the x, y, and z axes. Each point is a single reading. For small displacements (≤2 mm), the recorded chamber response remained within 2% of the CAX value (0.0 to 0.7% at 1 mm and 0.5 to 1.9% at 2 mm). Larger offsets produced progressively larger reductions: 1.7 to 4.0% at 3 mm, 3.0 to 7.0% at 4 mm and 4.9 to 12.0% at 5 mm, depending on the axis and the plan. The greatest sensitivity was observed along the x-axis with the new plan (12.0% at 5 mm), whereas z and y shifts produced smaller deviations (8.0% and 5.6%); an earlier run along x with a different plan gave only 3.0% at 4 mm and 4.9% at 5 mm. At the ±1.1% chamber band the chamber resolved offsets of 2 mm along x (3 mm on the older plan) and 3 mm along y and z. The repeat coefficient of variation (CoV) of the corrected charge was 0.19% (10 deliveries of one plan, phantom and chamber unchanged). The difference between the axes follows from the dose around the chamber point. The TPS dose averaged over the chamber volume predicts 5 mm reductions of 10.3% (x), 7.8% (z) and 4.3% (y) for a displacement towards positive IEC, against the 12.0%, 8.0% and 5.6% measured.

Table 3 Reduction of the chamber reading relative to the reference-position reading of the same plan, plan not adapted (%; one reading per offset). The detection limit is the smallest tested offset at which the reduction exceeds the ±1.1% chamber band.

Offset (mm)	**x (new plan)**	**x (older plan)**	**y**	**z**
1	0.7	0.0	0.2	0.1
2	1.9	0.5	0.8	0.8
3	4.0	1.7	1.7	2.7
4	7.0	3.0	3.3	4.9
5	12.0	4.9	5.6	8.0
Detection limit (mm)	2	3	3	3

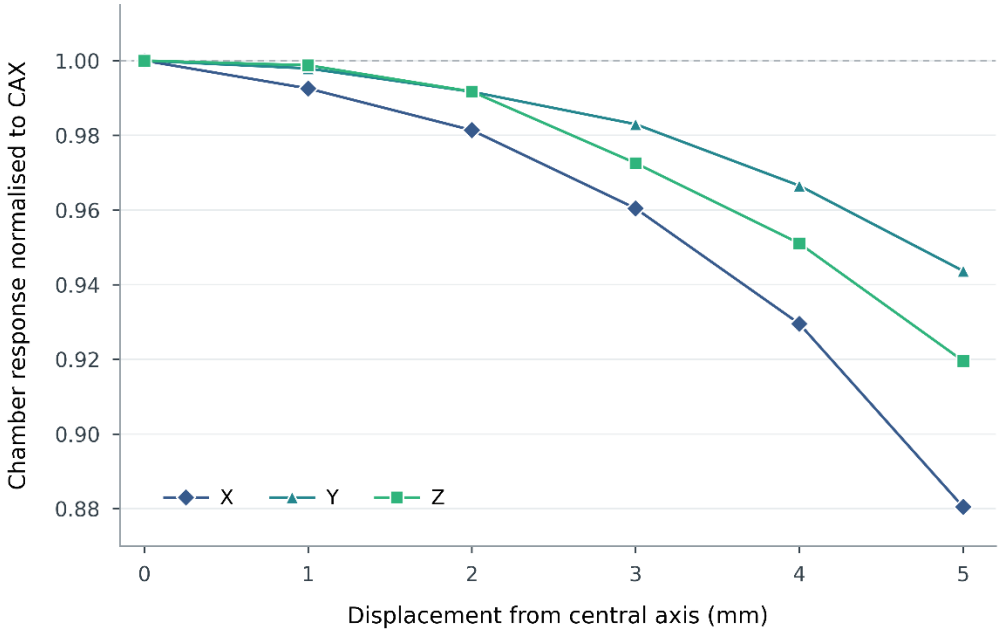


Fig. 8 Sensitivity of measurement to geometric misposition on each axis up to 5 mm in 1 mm increments (plan not adapted; x: new plan; one reading per offset)

Chamber absolute dose measurements under baseline conditions (16 setups) were within ±1% of the TPS dose to water (mean −0.25%, SD 0.44%, range −0.83 to +0.65%). For the 42 SSO adaptations along each individual axis and in combined directions the chamber read +0.2% (SD 0.6%, range −0.97 to +1.65%) against the TPS (R3; Figure 9; Table S2 in Online Resource 1); by axis the means were x +0.2% (n = 12), y +0.2% (n = 10), z +0.1% (n = 8) and combinations +0.2% (n = 12). Three points lay outside the chamber band of ±1.1% (plan labels as in Table S2): ADT24 (+1.65%), ADT45 (+1.34%) and ADT43 (+1.104%). Each point was also judged against its own uncertainty, the chamber term and the TPS statistical term of that point (k = 2, 1.2 to 2.1%, median 1.4%): 41 of 42 points agreed within it. ADT45 did not (difference +1.34%, 2.03 standard uncertainties); it is the only one of the 60 measured points (offsets, baselines, SAM and SWO) beyond two standard uncertainties. The two adaptations by other methods, SAM (morph only) and SWO (morph and weight optimisation), read −1.0% and 0.0%, both inside the band.

The offsets read higher than the baselines by +0.4% (95% confidence interval [CI] +0.1 to +0.7%; 42 offsets against the 16 baseline readings at the reference position). This depends on which baseline readings are used: against the mean of the baseline readings of each session (grouped by the workbook date cells) the difference is +0.3% (95% CI −0.1 to +0.7%, which includes zero), and it is therefore not claimed as an effect. As a sensitivity check, with the sessions defined instead by the recorded pressure and temperature, the difference is +0.45% (95% CI 0.00 to +0.89%). The central dose of the adapted plans rose relative to the baseline plan of their session by +0.8% measured against +0.5% in the TPS (42 adaptations).

The plan-side checks of the aperture positions, the whole-volume comparison and the departure correlations are in Online Resource 1.

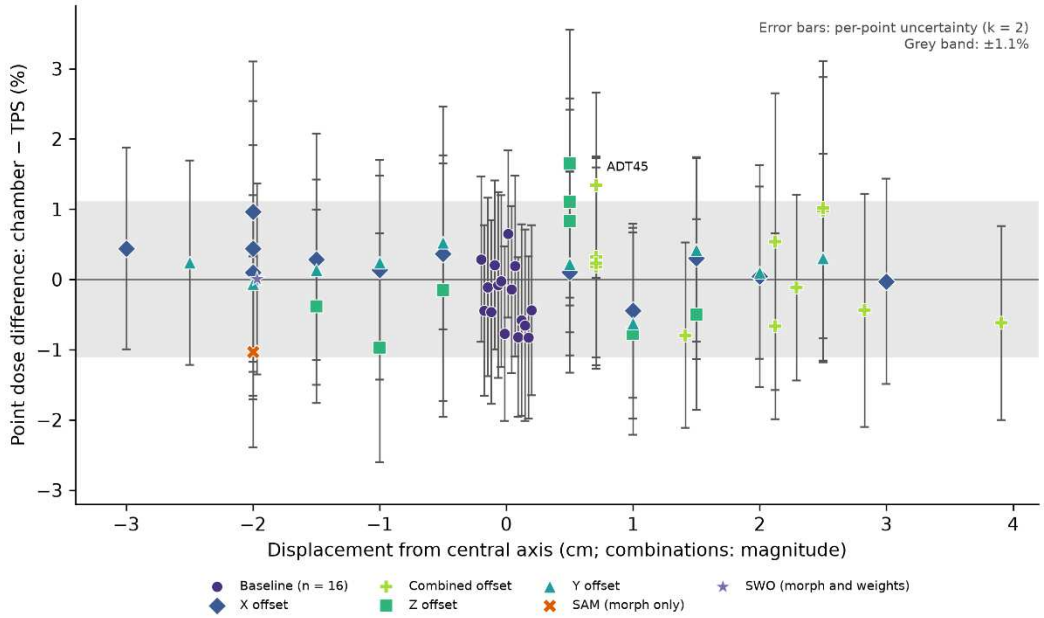


Fig. 9 Comparison of measured and TPS-calculated absolute dose (dose to water) for the 16 baseline setups and the 42 SSO adaptations, with the SAM and SWO adaptations. Error bars: per-point uncertainty (k = 2). Grey band: ±1.1%

Film measurements

Film-TPS comparisons at the baseline position demonstrated close agreement between measured and calculated dose distributions (profiles in the coronal film plane, Figure 10). All film-to-TPS and film-to-film comparisons passed the global 2%/2 mm gamma criterion (10% low-dose threshold, dose normalised to the maximum dose). The film-to-film comparisons used the maximum offset on all three adjusters, indicating good agreement of the adapted and reference plan for the displacements investigated.

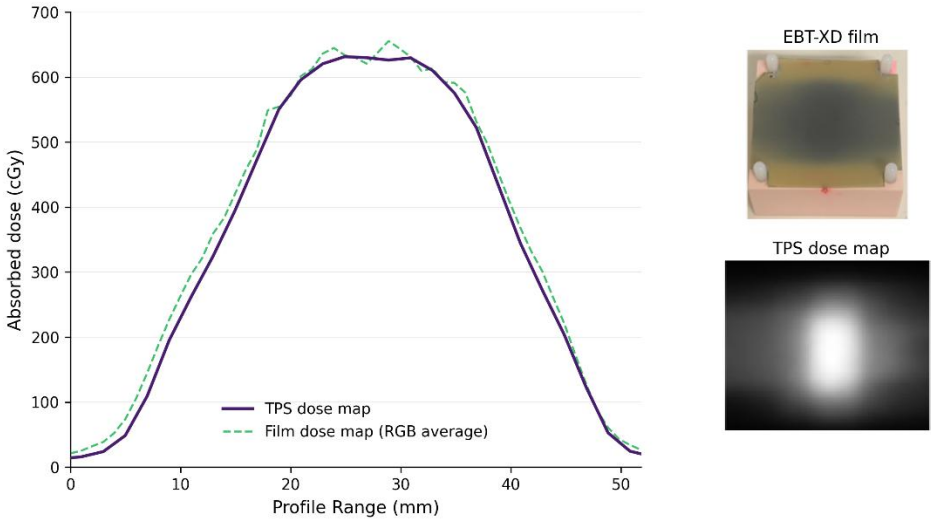


Fig. 10 Baseline film-to-TPS comparison showing close alignment and >99% gamma pass rate at 2%/2 mm

Film-to-TPS gamma comparisons were performed in the coronal, sagittal, and transverse planes. The largest discrepancies were confined to high-gradient regions near the build-up and penumbra, while central dose regions showed excellent concordance. Gamma analysis passed the 2%/2 mm criterion in all planes, confirming plan fidelity regardless of orientation.

Discussion

As shown in Table 2, the largest geometric contributors to uncertainty were the CT–MR fusion process (±0.5 mm) and MR geometric distortion (±0.47 mm), reflecting the dual challenges of multimodal registration and intrinsic MR system distortions. The latter was treated separately from the fusion process to ensure that acquisition-related effects were not conflated with registration performance, thereby maintaining transparency in the uncertainty budget. Measured mechanical contributors such as 3D-printed spacer accuracy (±0.4 mm) and couch position reproducibility (±0.2 mm) were comparatively minor, with the combined geometric uncertainty of ±0.82 mm (k = 2) corresponding to approximately one voxel dimension in the imaging system. From a dosimetric perspective, the combined chamber-based uncertainty of 1.1% (k = 2) is well within accepted clinical tolerances for absolute dose verification.

To further assess the practical implications of these findings, the sensitivity of the 3D PinPoint chamber to deliberate geometric misalignments was evaluated (Figure 8). The chamber detected offsets of 2 mm along x (3 mm on the older plan) and 3 mm along y and z at the 1.1% band; its response to smaller displacements was less distinct, with changes of at most 0.8% below these limits (Table 3). This behaviour reflects the interplay between the chamber's finite sensitive volume, the local dose gradient and modulation structure of the plan, and the measured dosimetric uncertainty of 1.1%, which is of the same order as the dose change resulting from a 1 or 2 mm positional error (0.0 to 0.7% at 1 mm and 0.5 to 1.9% at 2 mm). Consequently, misalignments below 2 mm along x and below 3 mm along y and z cannot be confidently resolved using ionisation chamber data alone, as any measured deviation may fall within normal dosimetric variability.

When chamber point doses were compared directly against the TPS across all offset directions (Figure 9), the chamber read +0.2% (SD 0.6%) against the TPS dose to water, with differences between −0.97 and +1.65% and 38 of the 42 points inside ±1%. This applied to both single-axis displacements and multi-axis combinations: at 41 of 42 points the chamber agreed with the adapted TPS dose within its per-point uncertainty. The exception, ADT45, lay at 2.03 standard uncertainties. The spread of the differences at offsets (SD 0.59%) was close to that at baseline (SD 0.44%). The adapted plans carried more dose at the chamber than the baseline plan of their session in the TPS, and the chamber read slightly more than that rise (+0.8% against +0.5%). The difference between offsets and baselines depends on which baseline readings are used and is not claimed as an effect. The aperture departures from a pure translation, which arise in the re-optimisation of the segments, are visible in the plan-side comparison (Online Resource 1) and are not resolved by the chamber. These findings confirm that the chamber provides reliable verification of absolute dose consistency, while also highlighting that its ability to discriminate smaller positional effects is inherently limited by spatial averaging.

When placed in the context of the total geometric uncertainty of ±0.82 mm, these results highlight both the robustness and the limitations of chamber-based verification: chambers provide reliable detection of larger geometric or dosimetric deviations but lack the spatial resolution to resolve smaller positional errors in high-gradient regions. This limitation underscores the complementary role of high-resolution dosimeters, such as

Gafchromic film, which are required to verify sub-millimetre positioning accuracy and to characterise subtle geometric effects that fall below the chamber's sensitivity.

Film dosimetry provided this additional layer of sensitivity, enabling high-resolution assessment of both baseline geometric accuracy and the robustness of the ATP workflow under introduced offsets. In the baseline comparison (Figure 10), film and TPS profiles were in close agreement, thereby establishing the baseline precision of the methodology. In contrast, the film-to-film comparisons, where multi-axis phantom offsets were applied, demonstrated that the ATP algorithm was able to reliably regenerate treatment plans that preserved dosimetric fidelity; all comparisons passed the global 2%/2 mm gamma criterion.

Importantly, because the internal configuration of the phantom remained unchanged, any deviations between reference and adapted films can be attributed solely to the geometric repositioning and the accuracy of the ATP algorithm in compensating for these changes. This finding directly supports the hypothesis that the ATP workflow should reproduce the reference plan in cases where no anatomical variation is present. Under these conditions, film confirmed that the ATP process faithfully recreated the intended dose distribution, even when the target was displaced off axis.

The robustness of these findings was further supported by film-to-TPS comparisons across all three orthogonal planes. Agreement between measured and calculated dose profiles was consistently high, with the largest deviations (<2 mm) confined to the build-up and penumbra regions where dose gradients are steepest. Central dose regions showed excellent concordance, with discrepancies typically within a few percent. Crucially, the consistency of results across coronal, sagittal, and transverse orientations demonstrates that the observed agreement is not plane-dependent but rather reflects the intrinsic accuracy of both the TPS modelling and the ATP adaptation process. This three-dimensional verification underscores that film can be used not only to identify subtle geometric deviations in a single orientation but also to confirm spatial fidelity across the full dose distribution.

Taken together, the chamber, film, and uncertainty analyses converge to demonstrate the robustness of the proposed methodology. The chamber offers absolute dose verification within clinically accepted tolerances, film provides the spatial resolution necessary to detect subtle geometric deviations, and the combined uncertainty analysis contextualises both within the MR-linac imaging environment. This multimodal approach ensures that both geometric precision and dosimetric fidelity can be interrogated comprehensively, thereby establishing a resilient QA framework capable of evaluating the day-to-day performance of ATP workflows in both phantom and clinical contexts.

Conclusion

This work presents a practical and robust methodology for evaluating the geometric and dosimetric performance of MR-linac adaptive workflows, with a focus on ATP. By integrating controlled geometric offsets, uncertainty quantification, and complementary verification tools, the approach provides a comprehensive means to assess system accuracy and stability.

CT–MR fusion and MR distortion were the main contributors to geometric uncertainty (<1 mm), and the registration read back 12 known spacer offsets within 0.6 mm. Over 42 ATP SSO adaptations the 3D PinPoint chamber read +0.2% (SD 0.6%) against the TPS dose to water, within its per-point uncertainty at 41 points (3 lay outside ±1.1%). Chamber measurements detected unadapted offsets of 2 mm along x (3 mm on the older plan) and 3 mm along y and z, so smaller deviations need film-based verification to resolve. Gafchromic film comparisons passed the global 2%/2 mm gamma criterion under offset conditions.

Together, these findings define a reproducible QA framework capable of characterising ATP workflow performance with high confidence. This methodology can be readily integrated into clinical practice and forms the foundation for future evaluation of ATS workflows and patient-specific adaptive scenarios.

Statements and Declarations

Funding: The authors declare that no funds, grants, or other support were received during the preparation of this manuscript.

Competing interests: The authors have no relevant financial or non-financial interests to disclose.

Ethics approval: This is a phantom study. The CT–MR registration offsets of the first 10 prostate patients treated on the MR-linac, used only to choose the maximum offset (Section 2.4), were reviewed as routine quality assurance, a quality activity exempt from Human Research Ethics Committee (HREC) review under institutional policy.

Consent to participate: Not applicable.

Consent for publication: Not applicable.

Data availability: The data that support the findings of this study are available from the corresponding author on reasonable request.

Code availability: The analysis scripts are available from the corresponding author on reasonable request.

Author contributions: Marchant Van der Walt: conceptualisation, methodology, investigation, formal analysis, writing – original draft. John Baines: supervision, writing – review and editing. Rick Franich: supervision, writing – review and editing.

References

1. Winkel D, Bol GH, Kroon PS et al (2019) Adaptive radiotherapy: the Elekta Unity MR-linac concept. Clin Transl Radiat Oncol 18:54–59. https://doi.org/10.1016/j.ctro.2019.04.001

2. Ingle M, White I, Chick J et al (2023) Understanding the benefit of magnetic resonance-guided adaptive radiotherapy in rectal cancer patients: a single-centre study. Clin Oncol 35(2):e135–e142. https://doi.org/10.1016/j.clon.2022.10.008

3. Christiansen RL, Dysager L, Hansen CR et al (2022) Online adaptive radiotherapy potentially reduces toxicity for high-risk prostate cancer treatment. Radiother Oncol 167:165–171. https://doi.org/10.1016/j.radonc.2021.12.013

4. Dona Lemus OM, Cao M, Cai B, Cummings M, Zheng D (2024) Adaptive radiotherapy: next-generation radiotherapy. Cancers 16(6):1206. https://doi.org/10.3390/cancers16061206

5. International Atomic Energy Agency (2019) Introduction of image guided radiotherapy into clinical practice. IAEA Human Health Reports No. 16. IAEA, Vienna

6. Jaffray DA, Siewerdsen JH, Wong JW et al (2002) Flat-panel cone-beam computed tomography for image-guided radiation therapy. Int J Radiat Oncol Biol Phys 53(5):1337–1349. https://doi.org/10.1016/S0360-3016(02)02884-5

7. Verellen D, De Ridder M, Storme G (2008) A (short) history of image-guided radiotherapy. Radiother Oncol 86(1):4–13. https://doi.org/10.1016/j.radonc.2007.11.023

8. Meyer J, Guckenberger M, Wilbert J, Baier K (2007) On the use of a hexapod table to improve tumour targeting in radiation therapy. In: Bioinspiration and robotics: walking and climbing robots. I-Tech Education and Publishing. https://doi.org/10.5772/5519

9. Schmidhalter D, Fix MK, Wyss M et al (2013) Evaluation of a new six degrees of freedom couch for radiation therapy. Med Phys 40(11):111710. https://doi.org/10.1118/1.4823789

10. Bissonnette JP, Balter PA, Dong L et al (2012) Quality assurance for image-guided radiation therapy utilizing CT-based technologies: a report of the AAPM TG-179. Med Phys 39(4):1946–1963. https://doi.org/10.1118/1.3690466

11. Van Dyk J (ed) (2020) The modern technology of radiation oncology, vol 4. Medical Physics Publishing, Madison. https://doi.org/10.54947/9781951134020

12. Lu L, Zhang Z, Qi P (2024) A review of online adaptive radiation therapy. Appl Radiat Oncol 13(4):17–25. https://doi.org/10.37549/ARO-D-24-00037

13. Lagendijk JJW, Raaymakers BW, Raaijmakers AJE et al (2008) MRI/linac integration. Radiother Oncol 86(1):25–29. https://doi.org/10.1016/j.radonc.2007.10.034

14. Corradini S, Alongi F, Andratschke N et al (2019) MR-guidance in clinical reality: current treatment challenges and future perspectives. Radiat Oncol 14:92. https://doi.org/10.1186/s13014-019-1308-y

15. Okamoto H, Igaki H, Chiba T et al (2022) Practical guidelines of online MR-guided adaptive radiotherapy. J Radiat Res 63(5):730–740. https://doi.org/10.1093/jrr/rrac048

16. Uno T, Tsuneda M, Abe K et al (2023) A new workflow of the on-line 1.5-T MR-guided adaptive radiation therapy. Jpn J Radiol 41(11):1316–1322. https://doi.org/10.1007/s11604-023-01457-4

17. Roberts DA, Sandin C, Vesanen PT et al (2021) Machine QA for the Elekta Unity system: a report from the Elekta MR-linac consortium. Med Phys 48(5):e67–e85. https://doi.org/10.1002/mp.14764

18. Snyder JE, St-Aubin J, Yaddanapudi S et al (2020) Commissioning of a 1.5T Elekta Unity MR-linac: a single institution experience. J Appl Clin Med Phys 21(7):160–172. https://doi.org/10.1002/acm2.12902

19. Woodings SJ, de Vries JHW, Kok JMG et al (2021) Acceptance procedure for the linear accelerator component of the 1.5 T MRI-linac. J Appl Clin Med Phys 22(8):45–59. https://doi.org/10.1002/acm2.13068

20. Bol GH, Lagendijk JJW, Raaymakers BW (2013) Virtual couch shift (VCS): accounting for patient translation and rotation by online IMRT re-optimization. Phys Med Biol 58(9):2989–3000. https://doi.org/10.1088/0031-9155/58/9/2989

21. Raaymakers BW, Jürgenliemk-Schulz IM, Bol GH et al (2017) First patients treated with a 1.5 T MRI-Linac: clinical proof of concept of a high-precision, high-field MRI guided radiotherapy treatment. Phys Med Biol 62(23):L41–L50. https://doi.org/10.1088/1361-6560/aa9517

22. Raaymakers BW, Lagendijk JJW, Overweg J et al (2009) Integrating a 1.5 T MRI scanner with a 6 MV accelerator: proof of concept. Phys Med Biol 54(12):N229–N237. https://doi.org/10.1088/0031-9155/54/12/N01

23. Thorwarth D, Low DA (2021) Technical challenges of real-time adaptive MR-guided radiotherapy. Front Oncol 11:634507. https://doi.org/10.3389/fonc.2021.634507

24. Van der Walt M, Crabtree T, Albantow C (2019) PLA as a suitable 3D printing thermoplastic for use in external beam radiotherapy. Australas Phys Eng Sci Med 42(4):1165–1176. https://doi.org/10.1007/s13246-019-00818-6

25. O'Brien DJ, Roberts DA, Ibbott GS, Sawakuchi GO (2016) Reference dosimetry in magnetic fields: formalism and ionization chamber correction factors. Med Phys 43(8):4915–4927. https://doi.org/10.1118/1.4959785

26. Tekin T, Blum I, Delfs B, Schönfeld AB, Poppe B, Looe HK (2022) The magnetic field dependent displacement effect and its correction in reference and relative dosimetry. Phys Med Biol 67(4):045004. https://doi.org/10.1088/1361-6560/ac4a41

27. Lewis D, Chan MF (2015) Correcting lateral response artifacts from flatbed scanners for radiochromic film dosimetry. Med Phys 42(1):416–429. https://doi.org/10.1118/1.4903758

Supplementary Files

This is a list of supplementary files associated with this preprint. Click to download.

- ESM1.docx